



## Evaluation and analysis of fracture modes in single composite basalt/epoxy fibres by photoelastic method and single fibre fragmentation test

Title	Evaluation and analysis of fracture modes in single composite basalt/epoxy fibres by photoelastic method and single fibre fragmentation test
Author(s)	Thornton, Eoghan;Ghabezi, Pouyan;Strain, Findhan;Harrison, Noel M.
Publication Date	2022-04-11
Publisher	Springer
Repository DOI	<a href="https://doi.org/10.1007/s12221-022-4597-y">10.1007/s12221-022-4597-y</a>

1 Evaluation and Analysis of Fracture Modes in single Composite  
2 Basalt/Epoxy Fibres by Photoelastic Method and Single Fibre  
3 Fragmentation Test

4 Eoghan Thornton<sup>3</sup>, Pouyan Ghabezi<sup>\* 1, 2, 3</sup>, Calvin Ralph<sup>4</sup>, Findhan Strain<sup>5</sup>, Noel M  
5 Harrison<sup>1, 2, 3, 6</sup>

6 <sup>1</sup> IComp Irish Composites Centre, Limerick, V94 T9PX, Ireland,

7 <sup>2</sup> I-Form Advanced Manufacturing Research Centre, Dublin, D04 V1W8, Ireland

8 <sup>3</sup> Mechanical Engineering, National University of Ireland, Galway, H91 TK33, Ireland,

9 <sup>4</sup> Mechanical Engineering, School of Engineering, Ulster University, Belfast, BT37 0QB

10 Northern Ireland,

11 <sup>5</sup> Director, Comeragh Composites, Belfast, BT9 6PP, Northern Ireland,

12 <sup>6</sup> Ryan Institute for Environmental, Marine and Energy Research, NUI Galway, Galway,  
13 H91 TK33, Ireland,

14 \* Corresponding author: Email: [pouyan.ghabezi@nuigalway.ie](mailto:pouyan.ghabezi@nuigalway.ie),  
15

16 **Abstract:**

17 In this work, the suitability of basalt fibres for uni-directional composite material  
18 applications, and adhesion between the fibres and the matrix they are embedded in  
19 have been investigated. A single fibre fragmentation test was carried out on 13µm  
20 diameter basalt fibres embedded in a dog-bone epoxy matrix. Photoelastic analysis  
21 was used to observe different fracture mechanisms in a single fibre composite  
22 sample and fibre breaks during testing. A theoretical model based on a Griffith's  
23 fracture mechanics approach was used to determine the fibre-matrix interfacial  
24 shear strength, which is a measurement of the level of adhesion between the fibre  
25 and the matrix. It was also used to predict the fibre fragment axial stress and the  
26 fragment interfacial shear stress, both as functions of axial position on the fibre. A

27 finite element model was developed to simulate the fibre fracture process, and the  
28 redistribution of stresses in the fibre and the local region surrounding a fibre break.  
29 The developed experimental procedure was successful in that stress-induced  
30 birefringence was observed in the tested samples, as well as the characteristic shear  
31 stress light fringes that occur in the regions surrounding fibre fractures. Also, there  
32 were some similarities between the finite element model results and the theoretical  
33 predictions. The critical fibre length,  $l_c$  was measured as 0.752 mm, whereas this  
34 value was calculated 0.6708 mm from finite element predicted interfacial shear  
35 stress distribution for fibre fragment. A combination of all three types of failure  
36 modes was recorded across the samples that were tested, while only a single failure  
37 mode was observed in the finite element model. According to the theoretical  
38 model, for a given set of parameters and constant stress with only the fibre length  
39 varying, the axial stress in the fibre reduces as the fibre gets smaller.

40 Keywords: Basalt fibre, Photoelastic, Fracture mode, Single Fibre Fragmentation  
41 Test, **Finite Element Modeling.**

## 42 1. Introduction

43 Today, basalt fibres can be considered the ‘new-comer’ to the composite industry. There  
44 is a wide range of material properties associated with basalt fibres which make it a desirable  
45 composite material. Some research has been done on fracture behaviour of composite  
46 materials to characterize their strength and resistance against different loadings [1]. An  
47 important characteristic of uni-directional composites is the level of adhesion at the interface  
48 between the fibre and the matrix. When uni-directional composites are subjected to a tensile  
49 load parallel to the fibre direction, stress is transferred from the matrix to the fibre via shear  
50 [2]. As the load increases, the fibre fractures into smaller lengths. At a certain point, the fibres  
51 are unable to fracture any further, as they essentially lose their load-bearing capacity. This

52 point is called fibre saturation, and the fibre fragment length at this point is known as the  
53 critical fibre length. The critical transfer length is required for the interfacial shear stress to  
54 load the fibre to its fracture stress. Fibres with a shorter length than this embedded in the matrix  
55 will pull out. One interesting feature of composites containing chopped fibres is that they are  
56 almost as strong as those containing continuous fibres; providing the fibres exceed a critical  
57 length. Fibres shorter than the critical length will not carry their maximum load are thus unable  
58 to function effectively. Beyond the critical length, the fibres will carry an increasing fraction  
59 of the applied load and may fracture before the matrix especially if the matrix material has  
60 some ductility eg. a thermoplastic such as PEEK or a metal matrix. It is therefore necessary to  
61 determine what the critical fibre length is. Shear stress is used to transfer the applied load to  
62 the fibre - so that the fibre can do its job and the tensile stress that results from this in the fibre  
63 is not the same along the length of the fibre - in fact, it increases from zero at the free end to  
64 some arbitrary value in the middle of the fibre then decreases as towards the other free end. A  
65 high level of adhesion is desirable in a composite, as it represents a good stress transfer  
66 mechanism from the matrix to the fibre. This allows for a significant portion of the load to be  
67 borne by the fibres, which have a much higher tensile strength and modulus than the matrix  
68 [2]. Single-fibre fragmentation test (SFFT) is the most widely used to evaluate interface  
69 properties in single-fibre composites, due to its ease of testing, relatively simple preparation  
70 of samples [3]. Wang et al [4] have carried out an SFFT test on carbon fibre-epoxy single fibre  
71 composites. A finite element model of the fibre failure process was also developed. The finite  
72 element model created was a 2-D planar model of a short section of the fibre and the  
73 surrounding matrix, and it was assumed that the fibre and matrix are perfectly bonded. Van  
74 der Meer et al. [5] have presented a numerical investigation into one of the tests that has been  
75 proposed for measuring interfacial properties between fibre and matrix. They have introduced  
76 a new cohesive zone model with friction, as well as an original numerical framework for

77 modelling embedded fibres. Their research has generated new insight into the meaning of the  
78 single fibre fragmentation test, confirming the applicability of shear lag theory also in presence  
79 of multiple cracks, and emphasizing the relevance of matrix plasticity for the development of  
80 friction in the test. Sørensen [6] has developed a shear-lag model utilizing the relation for the  
81 loss in potential energy of Budiansky, Hutchinson and Evans for the analysis of single fibre  
82 fragmentation tests for the characterization of the mechanical properties of the fibre/matrix  
83 interface in composite materials. Stojcevski et al. [7] have carried out single fibre  
84 fragmentation, Iosipescu and short beam shear testing to evaluate the translatability and  
85 sensitivity of interfacial shear strength across micro-, meso- and macro-scale testing protocols.  
86 Humbert et al. [8] proposed an exact solution for the characterization of thermal stresses in a  
87 single-fibre composite of finite length that involves a particular solution that is added to a  
88 three-dimensional complementary displacement field which satisfies automatically the  
89 Navier's equations. Kant and Penumadu [9] have measured the fracture toughness of single  
90 Toray T700 polyacrylonitrile carbon fibres using focused ion beam (FIB) nano-fabrication  
91 techniques to induce controlled geometry of end notches with lengths 100 nm to 1  $\mu\text{m}$ . These  
92 fibres were subjected to axial loading with a nano-tensile testing system for evaluating mode  
93 I fracture behaviour. The influence of the basalt fibre's length and content on the fundamental  
94 mechanical properties of concrete has been investigated Sun et al. [10] using multi-scale  
95 simulation. A damage constitutive model was developed at the mesoscopic scale in accordance  
96 with the Mori-Tanaka homogenization theory and progressive damage theory to predict the  
97 composite material properties of basalt fibre reinforced concrete. At the macroscopic scale,  
98 the obtained material properties of basalt fibre reinforced concrete from mesoscopic were input  
99 into the finite element specimen model to simulate the mechanical performance of these  
100 materials. Sarasini et al., [11] have presented an experimental investigation of the effects of  
101 temperature and atmosphere on the tensile behaviour of basalt fibres. The properties of basalt

102 fibres range from somewhere between E and S-glass fibres to slightly better than S-glass. It is  
103 worth noting that the cost of manufacturing for basalt fibres is less than that for S-glass fibres,  
104 making it a potential replacement for S-glass fibres [12]. A study carried out at Leuven  
105 University, Belgium, compared unidirectional E-glass and basalt fibre composites with a fibre  
106 volume fraction of 40% by subjecting them to a three-point bending test and an interlaminar  
107 shear strength test. The basalt fibre composite strength was recorded as 13.7% higher than that  
108 of the E-glass fibre composite, while the basalt fibre composite stiffness was 17.5% greater  
109 than the stiffness of the E-glass fibre composite [13]. Meng et al [14] conducted a series of  
110 experiments to develop continuous basalt fibres using two natural forms of basalt. The average  
111 tensile strength of the fabricated continuous basalt fibres was 4.1GPa. They revealed that the  
112 amount of glass network modifier ( $\text{Na}_2\text{O} + \text{K}_2\text{O}$ ) has a negative correlation with the tensile  
113 strength of continuous basalt fibres. Sabet et al. [15] have investigated the tensile strength of  
114 basalt fibres at room temperature and also after exposure to 300, 350, 400, 450 and 500 °C in  
115 a furnace for durations of 5, 10, 15 and 20 minutes. The results showed that the residual  
116 strength of basalt fibres drastically decreases after 20 min exposure at 300 and 400 °C and is  
117 only about 57% and 35% of that of fibres at room temperature, respectively. Eslami Farsani et  
118 al. [16] have studied the effects of thermal cycles on hardness and impact resistance of three  
119 types of phenolic-matrix composites, phenolic resin reinforced with (1) woven basalt fibres,  
120 (2) woven carbon fibres and (3) hybrid of basalt and carbon fibres. Akhlaghi et al. [17] have  
121 shown the applicability of basalt fibre as a reinforcing material for metal matrix composites  
122 through various experimental works for thermal stability and mechanical properties.

123 In this work, the goal is to determine the tensile load-bearing capability and fracture  
124 behaviour of basalt fibres for composite material applications. Whilst the properties and cost  
125 of basalt fibres suggest that they are a good choice for composite fibres, more information is  
126 required on the quality of adhesion between the fibres and the matrix they are embedded in.

127 In this research, a single fibre fragmentation test was performed on single fibre basalt-epoxy  
128 dog-bone samples, with the objective of characterising the interfacial adhesion and critical  
129 fibre length in single basalt fibre through observing the different fibre failure modes via  
130 photoelastic methods. A theoretical model which uses Griffith's fracture mechanics approach  
131 was used to quantify the interfacial adhesion in terms of interfacial shear strength. Finally, a  
132 finite element model was created to simulate the fibre failure process, finding critical fibre  
133 length, and failure modes.

## 134 **2. Experimental**

### 135 **2.1. Experimental Testing**

136 For the experimental testing in this research, a single fibre fragmentation test was carried  
137 out. The photoelastic analysis method is the most common technique used to determine the  
138 stresses at which a certain break occurs. The objective of this technique is to observe stress-  
139 induced birefringence, which occurs in transparent materials which are optically non-isotropic,  
140 in the region surrounding a fibre break and matching it with the stress at which it occurred.  
141 For fibre breaks to be accurately matched with the stresses at which they occur, incremental  
142 loading must be implemented [18]. After the application of a load, the gauge length can be  
143 scanned for the presence of any new fibre breaks before applying the next incremental load.  
144 The fibre diameter of each sample also needed to be accurately measured to carry out  
145 theoretical calculations.

### 146 **2.2. Materials**

147 The samples tested in this research were supplied by Comeragh Composites, Northern  
148 Ireland. The samples consist of a single 13  $\mu\text{m}$  diameter basalt fibre embedded in a dog-bone  
149 shape epoxy matrix. The basalt fibres used were manufactured by Mafic, located in Kells, Co.

150 Meath, Ireland. The epoxy matrix used was a low viscosity, two-part epoxy resin (RS-M135  
151 with a slow hardener, RS-MH137), which is a product of PRF Composite Materials, Poole,  
152 Dorset, England (Table 1). In order to embed the single basalt fibres into the epoxy matrix, a  
153 dog-bone mould was designed and the single fibres were fixed in the middle of the mould  
154 (Figure 1) within a slight tensile load to make sure the fibre does not get bent during adding  
155 the epoxy and the hardener to the die ad curing process. Also, the approximate sample  
156 dimensions are shown in Figure 1.

157 **Suggested position for Table 1**

158 **Suggested position for Figure 1**

### 159 **2.3. Sample Preparation**

160 A simple sample holder was constructed from match-sticks, small pieces of plywood,  
161 foam, and a container to prevent the samples from being damaged or scratched. The first step  
162 taken at the outset of the experimental testing was to observe the samples under a microscope  
163 to view the fibre. While the fibres were visible to the naked eye under certain lighting  
164 conditions, and clearly visible using a magnifying glass, when viewed under a microscope the  
165 fibre could not be observed. This was due to microscopic imperfections on the epoxy,  
166 increasing the surface roughness and resulting in the epoxy being too opaque for the lens to  
167 penetrate it. Various levels of sample illumination were used to try and overcome this, such as  
168 cleaning them with isopropyl alcohol, followed by polishing them using a polishing  
169 compound, applying Isopropyl alcohol, polishing using a Parkside PABSW B2 10.8V, 1.3Ah  
170 electric drill with a mini polishing pad, etc., but the microscope lens was unable to focus on  
171 the fibre due to surface imperfections. Finally, the sample preparation procedure which  
172 resulted in the desired surface finish was carried out in a 'Beuhler Beta Grinder-Polisher'. The

173 polishing compound used with the sample was a ‘Beuhler Masterprep 0.05 Micron Diamond  
174 Polishing Suspension’. The samples were polished until the surface observed under the  
175 microscope was considered satisfactory.

#### 176 **2.4. Measurement Of Fibre Diameter**

177 The fibre diameters were measured using an Olympus toolmakers microscope. The fibre  
178 diameters were measured under an X40 Olympus MSPlan20 lens and an Infinity camera  
179 attached, using the ocular crosshairs and stage displacement output. To calibrate the Infinity  
180 camera with the Olympus X40 lens, measurements needed to be taken from a stage micrometer  
181 of known dimensions. The stage micrometer used consisted of squares with a period of 10 $\mu$ m,  
182 which were arranged in multiple arrays, each of which had a period of 500 $\mu$ m. Once an image  
183 of the micrometer stage had been captured with the Infinity camera, the ‘Calibration’ option  
184 was chosen in the Infinity Analyse software. The largest length possible was then measured  
185 for calibration.

#### 186 **2.5. Experimental Setup and Testing**

187 The experimental setup is illustrated in Figure 2, and the experimental protocol was based  
188 on Hunston et al., n.d [19]. The complete experimental setup consists of: a tensile tester to  
189 load the samples in small increments; a white light source to illuminate the samples; two  
190 linear polarisers to polarise the light from the light source travelling through the sample so  
191 that stress-induced birefringence can be observed; an Infinity 2 camera with an X100 lens  
192 for monitoring and imaging of the fibre and sample; and a jack device to give the operator  
193 control over the vertical displacement of the Infinity camera, so that the entire gauge length  
194 can be examined. The tensile tester used was a hydraulic Instron 8874 with a 1kN load cell.  
195 As suggested by the experimental protocol developed by Hunston et al., n.d. [19], a strain  
196 of 0.2% was desired for each step. For a gauge length of 20 mm, this is equivalent to

197 0.04mm. No indication of the ideal crosshead speed is given in the test protocol, but the  
198 work of Awal et al. [20] has shown that the best results were obtained at a speed of  
199 0.2mm/min. Once the test was initiated, the displacement reading was monitored until the  
200 displacement had increased by 0.04mm, at which point the crosshead was stopped. It is  
201 recommended [19] that each load hold increment last 10 minutes. This is to ensure that  
202 stresses in the matrix are transferred to fibre before commencing the next step. It is  
203 recommended that the sample be left for the first 8 minutes, with the final 2 minutes for  
204 checking the fibre for the occurrence of any new breaks. Once all samples had been tested,  
205 the fibres were analysed using the toolmaker's microscope to capture images of the fibre  
206 breaks and to record the fibre fragment lengths.

207 **Suggested position for Figure 2**

208 This section details how the finite element model was created and refined to generate an  
209 accurate simulation of the fibre break in the single fibre fragmentation process. This model  
210 does not simulate interfacial debonding or matrix damage. The following method is based on  
211 Wang et al. work [4] in 2010. The finite element software ABAQUS CAE was used to create  
212 the model, while the fibre breaks were simulated using the subroutine USDFLD. This stands  
213 for User Defined Field and was developed in MS Visual Studio 2013 using the programming  
214 language FORTRAN. Fibre and matrix in this research were considered to be homogeneous,  
215 isotropic, elastic materials [4]. The elastic material properties that were assigned to the fibre  
216 and the matrix are shown in Table 1. As modelling of a fibre repeatedly fracturing is non-  
217 linear, a small increment size was required to ensure that an accurate solution is obtained.  
218 Once the model and subroutine were running successfully, an increment convergence study  
219 was carried out. Using an unbiased mesh of the same size for each job, the increment size was  
220 gradually reduced. The Von Mises stress of the same three elements was taken from each job

221 to determine increment convergence. Von Mises stress was used here as it incorporates all the  
222 principal stresses for each element. Figure 3 shows the entire mesh used for the increment  
223 convergence study.

224 **Suggested position for Figure 3**

225 The ratio of fibre to matrix elements used was 2:1, as seen in figure 3. From the results  
226 of the increment convergence study, it was evident that the solution converges at  
227 approximately 8000 increments. This increment size was selected as the final increment size  
228 and was then used for the mesh convergence study and final solution. Only two boundary  
229 conditions were required in the initial step of this model; the upper left and right-hand corners  
230 of the upper matrix section were constrained in the U2, or Y, direction. This was to prevent  
231 vertical displacement during tensile displacement of the model. With respect to loading, a  
232 tensile displacement load was applied to both ends of the model to simulate straining. The total  
233 displacement loading applied to the model was equivalent to 5% straining of the model. As  
234 the application of the displacement load was required at a constant rate, the ABAQUS default  
235 amplitude ramp was not suitable. Instead, a tabular amplitude was created, to give a linear  
236 application of displacement. Two initial conditions were also required to be defined in the  
237 input file to successfully run this model, as they are not supported in ABAQUS CAE. The  
238 initial condition types used were 'FIELD' and 'SOLUTION'. FIELD is used to assign initial  
239 values of predefined field variables. This initial condition was used to set the value of the  
240 elastic modulus field variable at each fibre node to 1, representing an un-degraded elastic  
241 modulus. SOLUTION allows for the definition of the initial values of solution-dependent state  
242 variables. This was applied to the fibre elements, with the initial value set to 1. Similar to  
243 FIELD, the function of this initial condition was to ensure that the fibre modulus is not  
244 degraded prematurely. To increase the accuracy of modelling, meshing of both the fibre and

245 matrix part instances utilised the same element type; a 4-node bilinear plane stress  
 246 quadrilateral element, with reduced integration, and hourglass control (CPS4R). A mesh of  
 247 medium fineness was used for the increment study, to achieve a good balance between  
 248 accuracy and computational time. However, to obtain an accurate final solution, a mesh  
 249 convergence study was also required. The method by which convergence was verified was  
 250 slightly different than that used in the increment study, as element sizes will change with  
 251 different meshes. Instead, the maximum Von Mises stresses for each mesh were compared.  
 252 Firstly, several unbiased meshes coarser than that shown in figure 3 (4200 elements) were  
 253 created. For the creation of meshes finer than that in figure 3, edge seed biasing was applied  
 254 to the vertical matrix edges. The mesh bias direction was set towards the fibre. The minimum  
 255 seed size was gradually reduced until the mesh elements close to the fibre were approximately  
 256 the same height as the fibre elements. The minimum seed size was not reduced further as a  
 257 mismatch between fibre and matrix element height was not desired. The results of the mesh  
 258 convergence study show that mesh convergence occurs at 12750 elements.

259 The chosen theoretical model was that of Limin Zhou et al. [21], which is Griffith's fracture  
 260 mechanics approach to the problem. This model is simplified slightly in this research, as the  
 261 complete model requires knowledge of friction coefficients and residual clamping stresses due  
 262 to matrix contraction and thermal shrinkage, which could not be determined. The procedure  
 263 to determine the fibre tensile stress at the critical length and hence the interfacial shear strength  
 264 from the SFFT is relatively simple and is outlined below. For a certain applied stress,  $\sigma_a$ , the  
 265 fibre tensile stress,  $\sigma_f$ , as a function of fibre fragment axial position is determined from the  
 266 following relationship [22]:

$$\sigma_f(z) = \eta \left( \sigma_a - \sigma_a \frac{\cosh \sqrt{A_1} z}{\cosh \sqrt{A_1} L} \right) \quad (1)$$

267 For fibre fragments of critical length,  $2L = l_c$ . As  $\sigma_f(z)$  is maximised at the centre of the fibre  
 268 fragment ( $z = 0$ , the fibre midpoint), the value for  $\sigma_f$  at this point is regarded as the fibre  
 269 fragment tensile strength.  $A_1$  and  $\eta$  are defined as [22] (Figure 4):

$$A_1 = \frac{2[\alpha + \gamma - 2k(\alpha\nu_f + \gamma\nu_m)]}{(1 + \nu_m) \left[ 2\gamma R^2 \ln\left(\frac{R}{a}\right) - a^2 \right]} \quad (2)$$

$$\eta = \frac{1 - 2k\nu_m}{\alpha + \gamma - 2k(\alpha\nu_f + \gamma\nu_m)} \quad (3)$$

270 Where  $R$  is the radius of the matrix region affected by the fibre break and is measured from  
 271 experimental images, and  $k$ ,  $\gamma$ , and  $\alpha$  are defined as [22]:

$$k = \frac{\alpha\nu_f + \gamma\nu_m}{\alpha(1 - \nu_f) + 2\gamma + \nu_m + 1} \quad (4)$$

$$\gamma = \frac{a^2}{R^2 - a^2} \quad (5)$$

$$\alpha = \frac{E_m}{E_f} \quad (6)$$

272 Suggested position for Figure 4

273 The interfacial shear strength,  $\tau_i$ , is then determined using a modified Kelly-Tyson formula.

$$\tau_i = K \frac{\sigma_f(l_c)d}{2l_c} \quad (7)$$

274 Where  $K$  is a constant with a value of 0.75 as suggested by Ohsawa et al. [23].

275 The interfacial shear stress distribution along the fibre length Assuming a perfectly bonded  
 276 interface after fibre fracture as a function of axial position,  $\tau_f(z)$ , is defined as [22]:

$$\tau_f(z) = \frac{\alpha\sqrt{A_1}}{2} (\eta\sigma_a) \frac{\sinh\sqrt{A_1}z}{\cosh\sqrt{A_1}L} \quad (8)$$

## 277 5. Results and Discussion

### 278 5.1. Experimental Preparation Results

279 Table 2 shows the fibre diameter measurements taken using the Infinity 2 camera. Note  
280 that samples 4 and 5 contained two fibres. As there was no single fibre for measurement in  
281 these samples, they are marked n/a.

282 **Suggested position for Table 2**

283 From Table 2, it can be seen that of the nine samples that were prepared for incremental  
284 load testing, three samples were not suitable (samples 3, 4, and 5). Of the remaining six  
285 samples, two were not suitable for testing as the fibres contained within them had a diameter  
286 of  $\sim 15\mu\text{m}$  (samples 8 and 9). A further sample (sample 1) was deemed unsuitable due to  
287 internal imperfections in the matrix which made it impossible to clearly view the fibre under  
288 polarised light. This left three samples remaining for incremental load testing (samples 2, 6,  
289 and 7). The samples which were not considered suitable for testing were subjected to a tensile  
290 test with continuous loading (samples 1, 4, 8, and 9).

## 291 **5.2. Testing Results**

292 Figure 5 displays the force and displacement values that were recorded after the completion  
293 of each incremental loading step along with the total number of fibre breaks that were observed  
294 after the completion of each loading step (Table 3).

295 **Suggested position for Figure 5**

296 The load and displacement values were recorded from the Instron control interface. The  
297 lower values for sample 6 relative to samples 2 and 7 is a result of a software issue during  
298 testing which resulted in the loss of data for the first few incremental loads. For this reason, as  
299 well as no fibre fractures being observed during testing or when using the toolmaker's  
300 microscope to measure fibre fragment lengths, sample 6 was excluded from further analysis.

301

Suggested position for Table 3

302 Figure 6 shows images taken of sample 2 during progressive stages of the increment  
303 loading. As the images obtained during loading are similar for all samples, only sample  
304 2 will be presented in detail. The average width of this sample was 3.917 mm, and this is  
305 marked in Figure 6 as a reference measurement. As different wavelengths/colours of light  
306 have different refractive indices, and due to the out-of-phase nature of the two light  
307 components, the colours of light in the components will undergo both destructive and  
308 constructive interference, resulting in the observed interference pattern. Figure 7  
309 illustrates a uniform birefringent colour (stress-induced birefringence) in the gauge  
310 length, representing a single stress state (tensile stress) of sample 2 at various loading  
311 stages. Figure 8 shows samples 1, 4, 8, and 9 (continuous loading) after failure. As  
312 mentioned previously, there were imperfections present in sample 1. In fact, of the nine  
313 samples, five (including sample 1) contained similar imperfections that made monitoring  
314 of the fibre during testing virtually impossible. The continuous loading of sample 1 was  
315 monitored using the Infinity camera and recorded to observe what occurs to these  
316 imperfections under loading. Several still images from the video are presented below in  
317 Figure 9.

318

Suggested position for Figure 6

319

Suggested position for Figure 7

320

Suggested position for Figure 8

321

Suggested position for Figure 9

322 Transverse microcracks were observed on the surfaces of the samples after testing,  
323 which is indicative of the occurrence of fracture failure mode I (Figure 10) which was  
324 expected due to the nature of the tensile test. The presence of these microcracks, which  
325 were not present before testing, made it significantly more difficult to locate the fibre in the  
326 sample.

327 **Suggested position for Figure 10**

328 As mentioned above, there were micro imperfections present in numerous samples.  
329 Sample 1 was observed to see what happened to these imperfections under loading. It  
330 appeared that they grew in size and became more birefringent as the load increased. This is  
331 illustrated in Figure 9. These imperfections were even in samples where the fibre was  
332 monitored (Figure 6), although not to the same extent as other samples. Voids may form  
333 during the curing process. Polymerisation increases the mechanical properties of the resin,  
334 which coincides with volumetric shrinking. If a resin is cured in a constrained mould, which  
335 is likely the case with the samples used in this testing, it can adhere to the walls of the  
336 mould, which induces tensile stresses. If these tensile stresses exceed the epoxy resin  
337 strength at a given stage of curing, voids will form [24]. This is a possible explanation for  
338 the presence of micro imperfections. The presence of white spots under polarised light is  
339 akin to crazing in polymers. The fact that when monitored under increasing load and  
340 polarised light they increase in size suggests that they are indeed voids. This could also  
341 explain why numerous samples failed near or at the end of the gauge length. Failure in these  
342 regions is not thought to be due to a combination of stress states in these areas, as Figure 7  
343 shows a uniform birefringent colour in the gauge length, representing a single stress state  
344 (tensile stress). As it can be seen, the colour diffraction trend has changed from load  
345 increment 14 (Figure 6 -D) to increment 18 (Figure 6 -E), a reason for this complies with

346 local shear stresses which occur in the interface of fibre and matrix surrounding. There are  
347 a number of stresses present at the ends of the gauge length, which is evident by the multiple  
348 light fringes visible in Figure 9 (Right). These fringes can be used to determine the principal  
349 stresses and their directions, however doing so would have no benefit to this research as the  
350 region of interest is the gauge length. It is postulated that failure in these regions  
351 surrounding the end of the gauge length may be due to the coalescing of these voids which  
352 introduces a weak spot in the sample for failure to initiate. The fact that several samples  
353 fail in the region at or very close to the gauge length marker (Figure 8) could suggest that  
354 there is some feature in one of the moulds used which facilitates the formation of these  
355 voids in this particular region.

### 356 **5.3. Fibre Fracture Results**

357 Table 4 presents the number of breaks that were found using the toolmaker's microscope,  
358 as well as the fragment length. Table 5 then displays the failure mode associated with each  
359 break. Mode (a) represents a strong interface, with the fibre break propagating into the matrix  
360 and creating a disc-shaped transverse crack with little or no interfacial debonding. Mode (b)  
361 also represents a strong interface, but for a matrix that has a relatively lower shear strength  
362 capability than tensile strength. This mode may also be accompanied by interfacial debonding.  
363 Mode (c) is the result of a weak interface, with the fibre fracture accompanied by interfacial  
364 debonding in the region surrounding the break. Mode (a) is the desirable failure mode, as it  
365 represents the highest level of adhesion between the fibre and matrix, and hence the most  
366 efficient stress transfer from the matrix to the fibre.

367 **Suggested position for Table 4**

368 **Suggested position for Table 5**

369 Figure 11 illustrates the different fractures that were recorded in the samples. Not every  
370 fracture is presented here as some are quite similar. Table 5 and Figure 11 show that a  
371 combination of all three types of failure modes was recorded across the samples that were  
372 tested, with sample 9 presenting all three failure modes. This was an unexpected  
373 observation as it indicates a significant variation in fibre-matrix adhesion in a small area.  
374 This would be undesirable in a composite material, as it would result in certain regions  
375 pertaining to good stress transfer from the matrix to the fibre, whereas other regions in close  
376 proximity may be characterised by poor stress transfer. In these regions of poor stress  
377 transfer, the fibre is debonded from the matrix, and the fibre load-bearing capacity is  
378 dramatically reduced [22]. This increases the load carried by the matrix in that region. This  
379 variation in the level of adhesion may lead to the concentration of stress in certain areas of  
380 the matrix, which would result in premature failure of the composite in those areas, where  
381 the failure is governed mainly by the properties of the matrix material. However, except for  
382 sample 9, fibre failure mode (c) was not observed in any other samples. Failure modes (a)  
383 and (b) were distributed almost equally across all samples, which suggests a good  
384 interfacial bonding between the fibre and the matrix. It is worth noting that of the samples  
385 which were tested under polarising light (samples 2 and 7) with two fibre breaks observed  
386 visually, upon examination under a microscope three and four fractures were detected in  
387 samples 2 and 7, respectively. By comparing the failure modes of each break in these  
388 samples and the length of the fragments between them with the length between the breaks  
389 observed experimentally, it was concluded that all breaks that were observed  
390 experimentally were of failure mode (b).

391 **Suggested position for Figure 11**

392 This observation can be explained as follows. According to [24], failure mode (b) is  
393 characterised by a matrix that has a relatively lower shear than tensile strength capability.  
394 When a fibre fractures and strain energy is released and propagates through the local matrix  
395 region, the matrix is subject to local shear deformation as a result of failure mode (b). Failure  
396 mode (b) is often accompanied by a ‘butterfly’ shaped fracture as a result of this shear failure.  
397 Local shearing of the matrix about the fracture deforms the polymeric chains, which gives rise  
398 to multiple refractive indices as a result of molecular directional anisotropy. This is reinforced  
399 by the examination of Figure 6 (H), which shows a close-up image of the fracture shear stress  
400 birefringent patterns. It is observed in this figure that, if the fibre is taken as an axis at  $0^\circ$ , the  
401 birefringent shear stresses act approximately in the area from  $315^\circ$  to  $45^\circ$  (anti-clockwise direction)  
402 and  $135^\circ$  to  $225^\circ$  (anti-clockwise direction). This shows alignment with shear bands which suggests  
403 local shear yielding has occurred. However, in failure mode (a), there is a greater level of  
404 adhesion between the fibre and matrix. As strain energy is released after fracture, it results in  
405 a transverse crack that propagates perpendicular to the fibre axial direction. As the polymeric  
406 chains are broken by the crack, rather than deformed, this significantly reduces the  
407 deformation of the polymeric chains, hence the lack of stress-induced birefringence. With  
408 respect to samples 4 and 6 where no fibre breaks were observed, it is thought that the presence  
409 of two fibres in sample 4 influenced the fracture response. With sample 6, it is believed that  
410 the malfunction of the software had an impact on the loading of the sample. The formation of  
411 each failure mode depends on the interfacial properties of fibre and matrix, the presence of  
412 voids in the vicinity of the fibres, manufacturing quality, and consequently shear properties.

#### 413 **5.4. Processed Results**

414 Table 6 gives information on testing temperature, and mechanical properties relating to  
415 each test.

416

Suggested position for Table 6

417 Stress-strain experimental results for samples loaded incrementally (samples 2 and 7) are  
418 derived, while samples 1, 4, 8, and 9 are subjected to continuous loading.

#### 419 **5.5. Finite Element Model Results**

420 Figure 12 to Figure 15 (Left) show the S11 stress component in the FE model before and  
421 after each break event, while Figure 12 to Figure 15 (Right) plot the axial stress state in the  
422 fibre/fibre fragments against the length of the fibre before and after each fibre break event.  
423 The regions where the curves dip are the locations of fibre breaks. The line colours used in the  
424 graphs to represent the fibre stresses after fibre fracture for a certain break event are also used  
425 to represent the fibre stresses before fibre fracture for the following break event. This allows  
426 for an easy comparison of fibre stresses in different break events. As evident from the right  
427 side of Figure 12 to Figure 15 when a fibre fractures into two fragments, the maximum stresses  
428 in these fragments are reduced. Once one of these fragments fractures into a further two  
429 fragments, the maximum stresses in these two fragments are less than any other fragments  
430 previously. This is analogous to the reduction of the fibre tensile strength with decreasing  
431 fragment length. At what point the fibres stop fracturing in the FE model, this could be taken  
432 as an estimate of the critical length.

433

Suggested position for Figure 12

434

Suggested position for Figure 13

435

Suggested position for Figure 14

436

Suggested position for Figure 15

437 There are several limitations associated with model, which are a result of some assumptions  
438 made during the modelling process. The only failure mode observed in the model is (b),  
439 because: a perfectly bonded interface was assumed with no relative motion between the fibre  
440 and matrix, which does not allow for interfacial debonding (failure mode (c)); no damage  
441 model for the matrix was developed, and therefore no transverse cracks could propagate into  
442 the matrix (failure mode (a)). The shear stresses present in the entire model are shown in Figure  
443 16. The interfacial shear stress at the fibre fragment interface was determined by creating a  
444 node path along one edge of a fibre fragment. The shear stress distribution along the fragment  
445 interface is plotted in Figure 17. The model accurately captures the shear stress distribution  
446 into the matrix about a fibre break, which is clearly evident when Figure 16 is compared with  
447 the experimental fracture shear stress distribution in Figure 6 (D). A butterfly-shaped  
448 distribution is observed, which is characteristic of failure mode (b). The model has also been  
449 able to successfully plot the shear stress distribution along a fibre fragment interface.

450 **Suggested position for Figure 16**

451 **Suggested position for Figure 17**

452 These findings show that the shear stress along the interface is zero at the fragment ends  
453 and is maximised a short distance from the fragment end before gradually decaying to zero at  
454 the fibre fragment midpoint. Using eq. (7), the interfacial shear strength for the fibre fragment  
455 shown in Figure 17 can be determined. Fibres shorter than the critical length will not carry  
456 their maximum load are thus unable to function effectively. Beyond the critical length, the  
457 fibres will carry an increasing fraction of the applied load and may fracture before the matrix  
458 especially if the matrix material has some ductility eg. a thermoplastic such as peek or a metal  
459 matrix. It is therefore necessary to determine what the critical fibre length is. The critical fibre  
460 length is defined as the shortest fibre fragment which can fracture with the application of stress

461 [25]. In other words, it is defined as the minimum length at which the centre of the fibre reaches  
462 the ultimate (tensile) strength  $\sigma_f$ , when the matrix achieves the maximum shear strength  $\tau_m$ .  
463 The critical fibre length,  $l_c$ , therefore, was taken as the distance spanned by the curve in Figure  
464 17, which is 0.6708 mm, and  $\sigma_f(l_c)$  is the maximum value of the third green peak from the  
465 right in Figure 15, which is 2620 MPa. The resulting interfacial shear strength is presented in  
466 table 7 to allow for comparison with theoretical predictions. The FE model developed was  
467 considered successful in almost all aspects, based on the objective of the model and the  
468 assumptions made. It successfully models the fracture of the fibre into successively smaller  
469 fragments through the application of a displacement load to the matrix only, where internal  
470 matrix stresses are transferred to the fibre via shear. The maximum fibre tensile stress is  
471 located at the centre of the fibres, which is the point of fracture once the failure criterion is  
472 reached. This is shown in the plots of fibre axial stress in this section. This is the expected  
473 fracture location in experimental testing in the absence of fibre imperfections. However, in  
474 reality this is not always observed. In basalt fibres imperfections can occur as a result of  
475 cooling due to thermal contraction [12]. Some of the minerals that constitute basalt have  
476 different melting temperatures [26], which can also influence the uniformity of fibres when  
477 cooling.

## 478 **5.6. Theoretical Results**

479 Generation of results using the chosen theoretical model required knowledge of the  
480 following parameters:  $l_c$ , the critical fibre length,  $a$ , the fibre radius,  $R$ , the radius of the  
481 matrix region affected by the fibre fracture, and  $\sigma_a$ , the applied stress. Only results for  
482 samples 2 and 7 are presented here, as they were the only samples where fibre fractures  
483 were observed during experimental testing. As it could not be determined if either sample  
484 2 or 7 reached saturation as only two fibre fractures were observed experimentally,  $l_c$  was  
485 taken as the minimum fibre fragment length that was recorded during single fibre  
486 fragment test.  $a$  was determined from the measurements given in table 2.  $\sigma_a$  was taken as  
487 the applied stress at the end of the step at which the second fibre fracture was observed.

488  $R$  was determined by measuring the images taken of samples 2 and 7. As  $R$  is defined as  
489 the radius of the matrix region which is affected by the fibre break, this can be taken as  
490 the radius of sheared region surrounding the fibre break. The diameter of each shear  
491 region was measured, and average value was determined to use in the calculations. With  
492 these parameters determined, eqs. (1) through (7) can be used to determine the interfacial  
493 shear strength and to plot the tensile and shear stress distribution along a fibre fragment  
494 for samples 2 and 7, assuming a critical length of 0.752 mm in both cases from  
495 experimental work ( table 4).

496 Table 7 gives the calculated interfacial shear strengths for the theoretical model and  
497 the FE model, while Figure 18 plots the tensile and shear stress distributions along a fibre  
498 fragment for samples 2 and 7. Figure 19 plots the axial stress distribution of the sample 7  
499 fragment shown in Figure 18 (C), along with the stress distributions for fibre of  
500 decreasing length that are otherwise of the same dimensions as sample 7 and are subject  
501 to the same loading conditions.

502 **Suggested position for Table 7**

503 **Suggested position for Figure 18**

504 The FE model assumes that the tensile strength of the fibre is constant, when in fact it  
505 decreases as the fibre length decreases, as illustrated in Figure 19. Figure 19 plots the  
506 theoretical axial stress distribution of the sample 7 fragment shown in figure 18-C, along with  
507 the stress distributions for fibre of decreasing length that are otherwise of the same dimensions  
508 as sample 7 and are subject to the same loading conditions. The initial opening displacement  
509 is also quite large for the first break and is not considered representative of actual fibre failure.  
510 This is a result of the failure criterion and the initial length of the fibre. Before fibre fracture,  
511 the fibre is quite long. As load is transferred to the fibre, the load increases, with the maximum  
512 load at the centre of the fibre. However, due to the length of the fibre, several elements at the  
513 centre have very similar stresses and exceed the failure criterion simultaneously. The model  
514 also fails to capture the decay of the fibre fragment axial stress to zero at the fragment ends.

515 This is because when the elastic modulus is degraded for certain elements, it does not go to  
516 zero, and hence the degraded elements still pertain some load-bearing capacity. Based on a  
517 comparison of Figure 18, it is evident that this model is able to determine the fibre axial stress  
518 as a function of axial position for different fibres and matrices. Figure 19 illustrates that for a  
519 given set of parameters and constant stress with only the fibre length varying, the axial stress  
520 in the fibre reduces as the fibre gets smaller. This model can capture the decaying of the  
521 fragment interfacial shear stress to zero as the axial position approaches the midpoint of the  
522 fibre. Unlike the FE model, and similar to many other theoretical models, the chosen model  
523 does not predict zero shear stress at the fibre ends, but rather maximises it. However,  
524 similarities between the values for shear stress in the FE model and those predicted by the  
525 theoretical model for similar fragment lengths are evident. The same cannot be said for the  
526 comparison between the theoretical fibre fragment axial stress and that in the FE model, due  
527 to limitations of the FE model, which were discussed in the previous section.

528 **Suggested position for Figure 19**

## 529 **7. CONCLUSION**

530 A SFFT test was carried out on 13  $\mu\text{m}$  basalt fibre-epoxy composite samples, and fracture  
531 behaviour (mode) of different samples were indicated. A Griffith's fracture mechanics  
532 approach was used to predict the interfacial shear strength, and the axial and shear stress  
533 distribution in a fibre fragment as a function of fragment axial position. The developed  
534 experimental procedure in this work was considered a success, although there were challenges  
535 with obtaining the desired results, in that stress-induced birefringence was observed in the  
536 tested samples, as well as the characteristic shear stress light fringes that occur in the regions  
537 surrounding fibre fractures. A 2-D planar FE model was also created to simulate the problem.  
538 The primary conclusions of the study are:

- 539 • From experimental tests, the critical fibre length,  $l_c$ , was measured as 0.752 mm,  
540 whereas this value was calculated 0.6708 mm from FE predicted interfacial  
541 shear stress distribution for fibre fragment.
- 542 • It appeared that micro imperfections in the matrix surrounding fibres grew in  
543 size and became more birefringent as the load increased.
- 544 • A combination of all three types of failure modes (mode a, mode b, and mode  
545 c), were recorded across the samples. In contrast, only a single failure mode was  
546 observed in the model, failure mode (b), due to the lack of interface properties  
547 in the model or a damage model for the matrix.
- 548 • The FE model created was able to capture the transfer of stress from the matrix  
549 to the fibre via shear. The interfacial shear stress distribution along the fragment  
550 length was correctly predicted, with zero shear stress observed at both ends of  
551 the fragment, and at the midpoint.
- 552 • Theoretical fibre fragment interfacial shear stress as a function of fibre fragment  
553 axial position correctly captured the decay of shear stress to zero at the fibre  
554 fragment midpoint, but failed to predict zero shear stress at the fragment ends,  
555 instead maximising it.
- 556 • Some similarities between the FE model results and the theoretical predictions  
557 were observed.
- 558

## 559 **Declarations**

560 **Conflict of interest:** The authors declare that they have no known competing financial  
561 interests or personal relationships that could have appeared to influence the work reported  
562 in this paper.

## 563 **REFERENCES**

- 
1. F. Hatami, M.R. Ayatollahi, A.R. Torabi, Limit curves for brittle fracture in key-hole notches under mixed mode I/III loading based on stress-based criteria, *Eur. J. Mech. A Solids*, 85, 104089, 2021.
  2. S. Feih, K. Wonsyld, D. Minzari, P. Westermann, Testing Procedure for the Single Fiber Fragmentation Test, *Risø National Laboratory for Sustainable Energy, Technical University of Denmark, Denmark*, 1: 1-28, 2004.
  3. D. Tripathi, F.R. Jones, Single Fibre Fragmentation Test for Assessing Adhesion in Fibre Reinforced Composites, *J. Mater. Sci.*, 33(1): 1-16, 1998.
  4. X. Wang, B. Zhang, S. Du, Y. Wu, X. Sun, Numerical simulation of the fiber fragmentation process in single-fiber composites, *Mater. Des.*, 1980-2015, 31(5): 2464–2470, 2010.
  5. F.P. Van der Meer, S. Raijmaekers, I.B.C.M. Rocha, Interpreting the single fibre fragmentation test with numerical simulations, *Compos. Part A Appl. Sci. Manuf.*, 118: 259-266, 2019.
  6. B.F. Sørensen, Micromechanical model of the single fiber fragmentation test, *Mech. Mater.*, 104: 38-48, 2017.
  7. F. Stojcevski, T.B. Hilditch, L.C. Henderson, A comparison of interfacial testing methods and sensitivities to carbon fiber surface treatment conditions, *Compos. Part A Appl. Sci. Manuf.*, 118: 293-301, 2019.
  8. L. Humbert, F. Colpo, J. Botsis, An axisymmetric stress analysis in a single fibre composite of finite length under a thermal expansion mismatch, *Eur. J. Mech. A Solids*, 28(2): 257-265, 2009.
  9. M. Kant, D. Penumadu, Fracture behavior of individual carbon fibers in tension using nano-fabricated notches, *Compos. Sci. Technol.*, 89: 83-88, 2013.
  10. X. Sun, Z. Gao, P. Cao, C. Zhou, Mechanical properties tests and multiscale numerical simulations for basalt fiber reinforced concrete, *Constr. Build. Mater.*, 202: 58-72, 2019.
  11. F. Sarasini, J. Tirillò, M.C. Seghini, Influence of thermal conditioning on tensile behaviour of single basalt fibres, *Compos. B. Eng.*, 132: 77-86, 2018.
  12. K. Singha, A Short Review on Basalt Fibres, *Int. J. Text. Sci.*, 1(4): 19–28, 2012.
  13. A. Ross, Basalt Fibers: Alternative to Glass? <https://www.compositesworld.com/articles/basalt-fibers-alternative-to-glass>, (Accessed 15 February 2021).
  14. Y. Meng, J. Liu, Y. Xia, W. Liang, Q. Ran, Z. Xie, Preparation and characterization of continuous basalt fibre with high tensile strength, *Ceram. Int.*, 47: 9, pp 12410-12415, 2021.

- 
- 15 S. Sabet, F. Akhlaghi, R. Eslami Farsani, The Effect of Thermal Treatment on Tensile Properties of Basalt Fibers, *J. Ceram. Sci. Technol.*, 6(3): 245-248, 2015.
  - 16 R. Eslami-Farsani, M.R. Khalili, M. Najafi, Effect of Thermal Cycling on Hardness and Impact Properties of Polymer Composites Reinforced by Basalt and Carbon Fibers, *J. Therm. Stresses*, 36 (7): 684-698. 2013.
  - 17 F. Akhlaghi, R. Eslami-Farsani, SMM Sabet, Synthesis and Characteristics of Continuous Basalt Fiber Reinforced Aluminum Matrix Composites, *J. Compos. Mater.*, 47(27): 3379-3388, 2013.
  18. M.J. Rich, L.T. Drzal, , D.L. Hunston, G.A. Holmes, W.G. McDonough, Round Robin Assessment of the Single Fiber Fragmentation Test, Proceedings of the American Society for Composites 17th Technical Conference, West Lafayette, IN, 2002.
  19. D.L. Hunston, W.G. McDonough, G.A. Holmes, R. Parnas, Test Protocol for Single-Fiber Fragmentation Test, [http://www.hunstonscientific.com/index\\_htm\\_files/InterfaceRR.pdf](http://www.hunstonscientific.com/index_htm_files/InterfaceRR.pdf) (Accessed 12 February 2021)
  20. A. Awal, G. Cescutti, S.B. Ghosh, J. Müssig, Interfacial studies of natural fibre/polypropylene composites using single fibre fragmentation test (SFFT), *Compos. Part A Appl. Sci. Manuf.*, 42(1): 50–56, 2011.
  21. L. Zhou, J.K. Kim, C. Baillie, Y.W. Mai, Fracture Mechanics Analysis of the Fibre Fragmentation Test, *J. Compos. Mater.*, 29(7): 881–902, 1995.
  22. S. Deng, L. Ye, Y.W. Mai, H.Y.Liu, Evaluation of fibre tensile strength and fibre/matrix adhesion using single fibre fragmentation tests, *Compos. Part A Appl. Sci. Manuf.*, 29(4): 423–434, 1998.
  - 23 T. Ohsawa, A. Nakayama, M. Miwa, A. Hasegawa, Temperature dependence of critical fiber length for glass fiber-reinforced thermosetting resins. *J. Appl. Polym. Sci.* 22, 3203–3212. <https://doi.org/10.1002/app.1978.070221115>, 1978.
  24. E. Yongsung, B. Louis, M.Véronique, S. Paul, M. Jan-Anders, Stress-initiated void formation during cure of a three-dimensionally constrained thermoset resin, *Polym. Eng. Sci.*, 41(3): 492–503, 2004.
  25. D. Tripathi, A. Kettle, N. Lopattananon, A. Beck, F.R. Jones, Interface molecular engineering of carbon-fiber composites, *Compos. Part A Appl. Sci.*, 30(1):49-57, 1999.
  26. R. Gill, “Igneous rocks and processes: A practical guide”, 2<sup>nd</sup> ed. pp. 20-64, Wiley-Blackwell, Oxford, 2010.

Table 1: Material properties of basalt fibre and epoxy (material data sheets).

Property	13 $\mu\text{m}$ Basalt Fibre	Epoxy Resin
Elastic Modulus (MPa)	90,000	3,400
Tensile Strength (MPa)	3,100	75
Poisson's Ratio	0.26	0.33
Elongation at break (%)	3.5	5 – 6.5

Table 2: Results of fibre diameter measurements using Infinity 2 camera.

Sample No.	Avg. ( $\mu\text{m}$ )	Sample No.	Avg. ( $\mu\text{m}$ )	Sample No.	Avg. ( $\mu\text{m}$ )
1	13.20	4	n/a	7	12.31
2	13.09	5	n/a	8	15.27
3	damaged	6	13.40	9	15.07

Table 3: Fibre breaks vs load increment (F= failure occurred).

Load Increment	21	22	23	24	25	26	27	28	29	30	31	32
Fibre Breaks for sample 2	1	2	2	F								
Fibre Breaks for sample 6	0	F										
Fibre Breaks for sample 7	0	1	1	1	1	1	1	2	2	2	2	F

Table 4: Number of breaks and fibre fragment lengths in each sample.

Sample No.	No. of Breaks	Fragment Length (mm)			
		Break 1-2	Break 2-3	Break 3-4	Break 4-5
1	3	1.695	5.384	n/a	n/a
2	3	1.190	0.752	n/a	n/a
7	4	1.305	2.015	1.650	n/a
8	6	1.110	1.420	1.531	3.325
9	4	0.752	1.882	1.101	n/a

Table 5: Different failure modes of each break observed.

Sample No.	Fibre Break Failure Mode Type				
	Break 1	Break 2	Break 3	Break 4	Break 5
1	(b)	(b)	(a)	n/a	n/a
2	(a)	(b)	(b)	n/a	n/a
7	(b)	(a)	(b)	(a)	n/a
8	(b)	(a)	(a)	(a)	(a)
9	(c)	(a)	(b)	(b)	n/a

Table 6: Test temperatures and other testing values determined from data files.

Sample No.	Test Temp. (°C)	Max Load (N)	Max Disp. (mm)	U.T.S. (MPa)	Failure Strain (%)	Elastic Modulus (MPa)
1	20	402.67	1.31	72.93	6.56	1510.3
2	20	444.55	1.04	61.80	5.18	1455.4
4	19	419.58	1.06	68.39	5.32	1638.5
7	19	474.35	1.27	74.80	6.37	1670.0
8	20	484.82	1.28	82.45	6.39	1720.3
9	20	469.52	1.29	81.57	6.43	1740.6

Table 7: Theoretical interfacial shear strength values.

Sample No.	2	7	FE model
$\tau_i$ (MPa)	9.0451	9.7708	19.0407

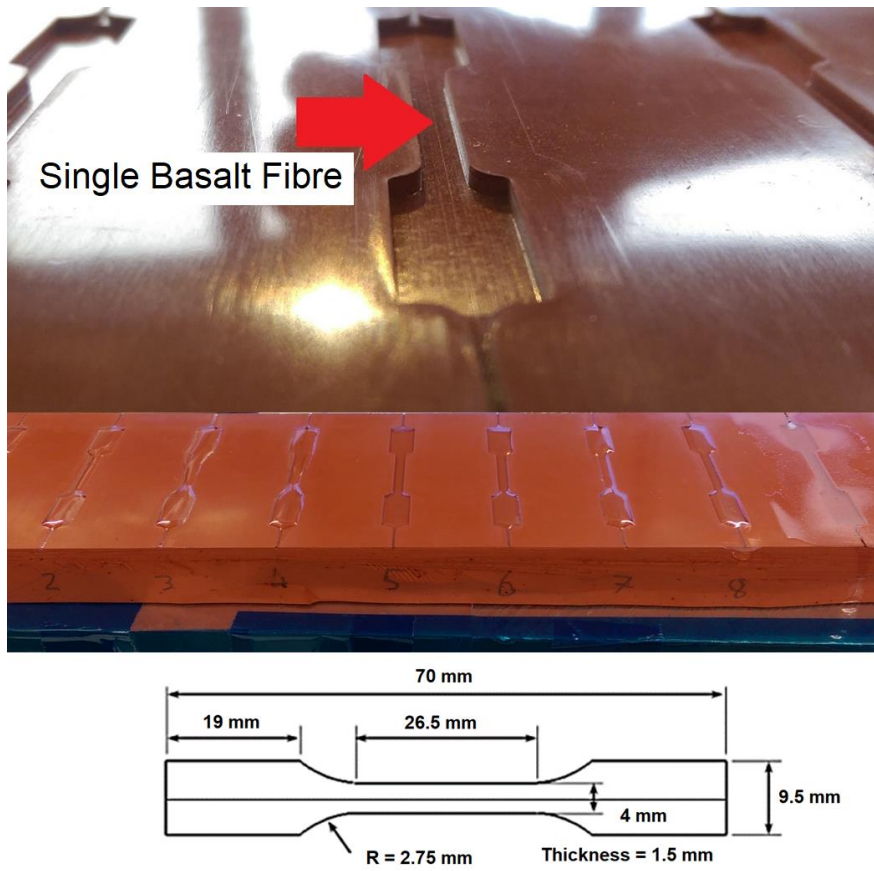


Figure 1: Sample manufacturing and approximate dimensions of samples.

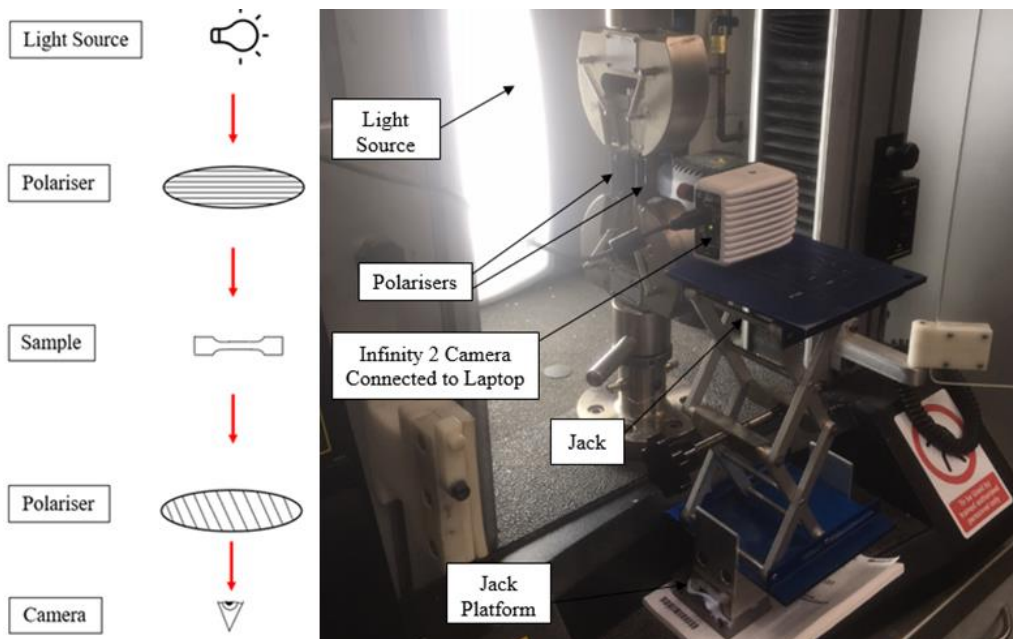


Figure 2: Experimental testing diagram and setup.

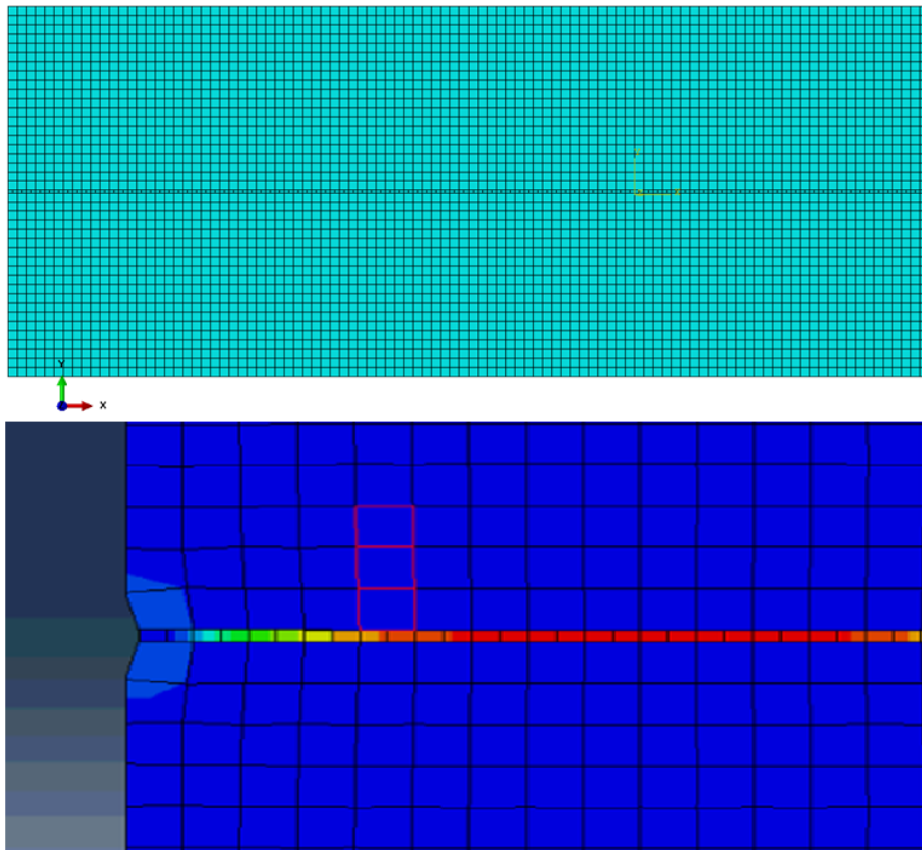


Figure 3: The increment convergence study.

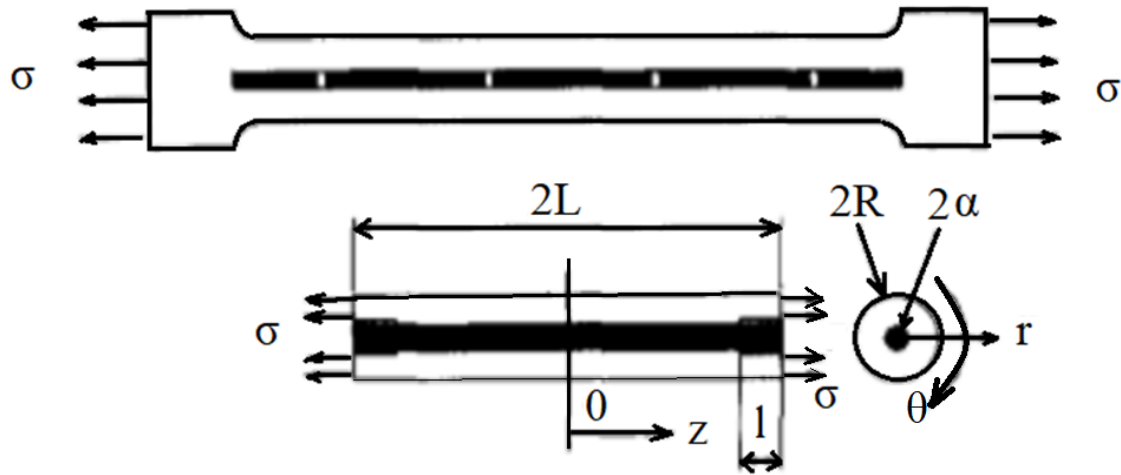


Figure 4: Schematic diagram of parameters required for theoretical model.

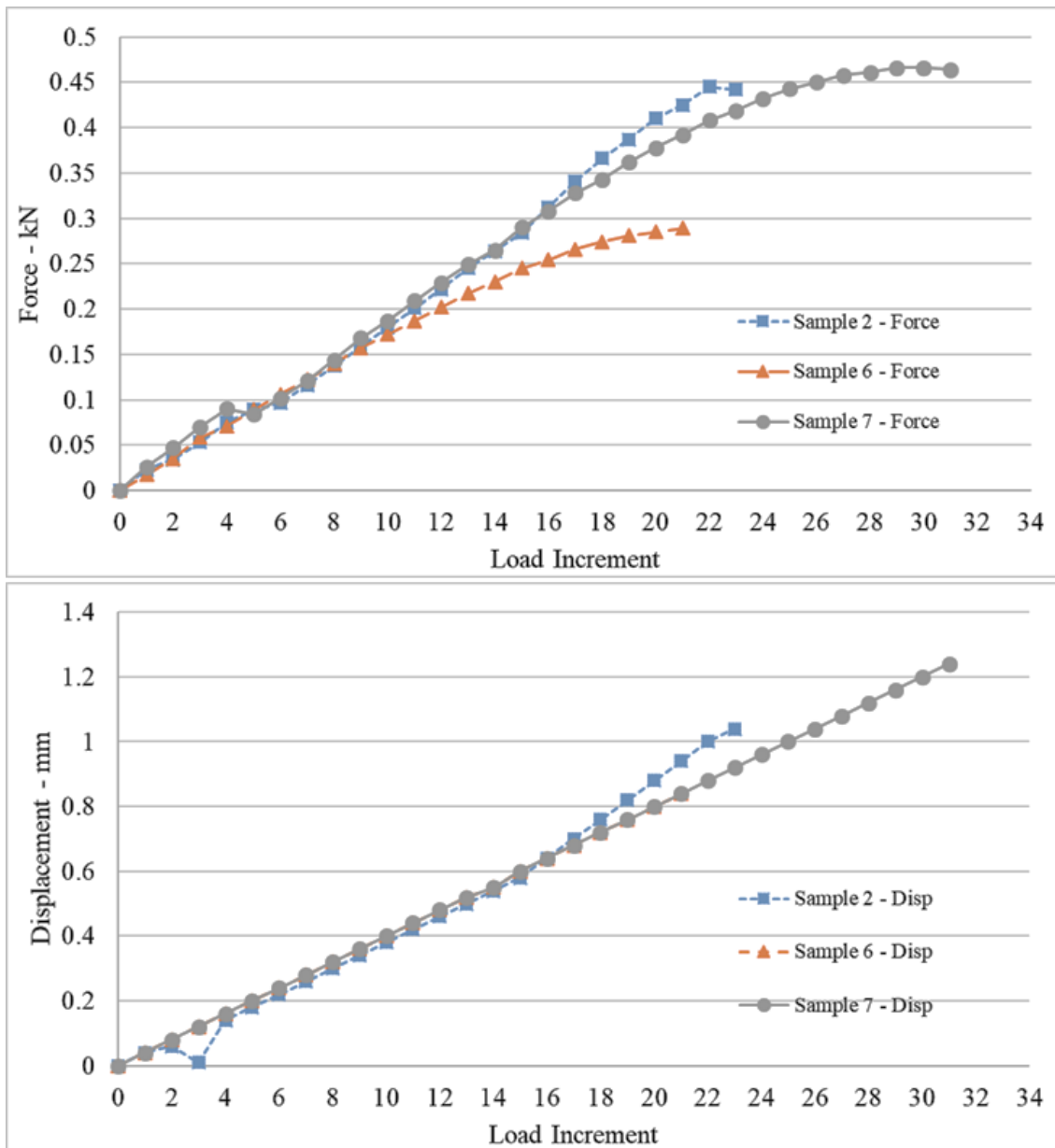


Figure 5: Recorded force and displacement values after each incremental loading step

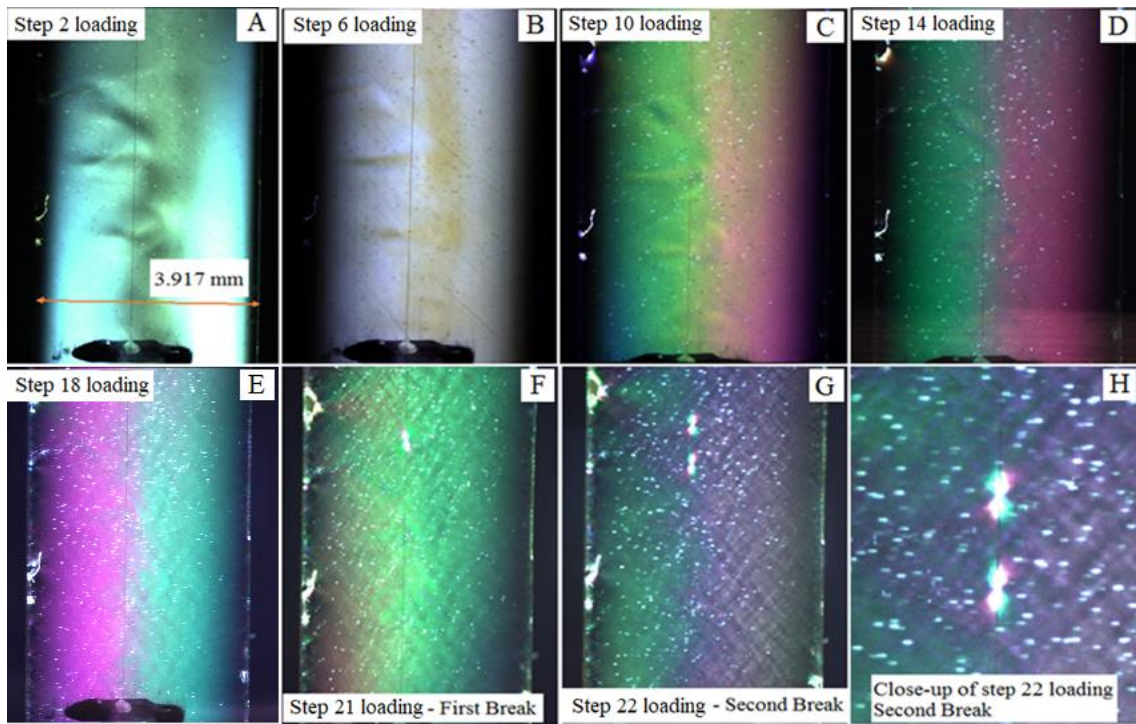


Figure 6: Sample 2 images in different loading steps.

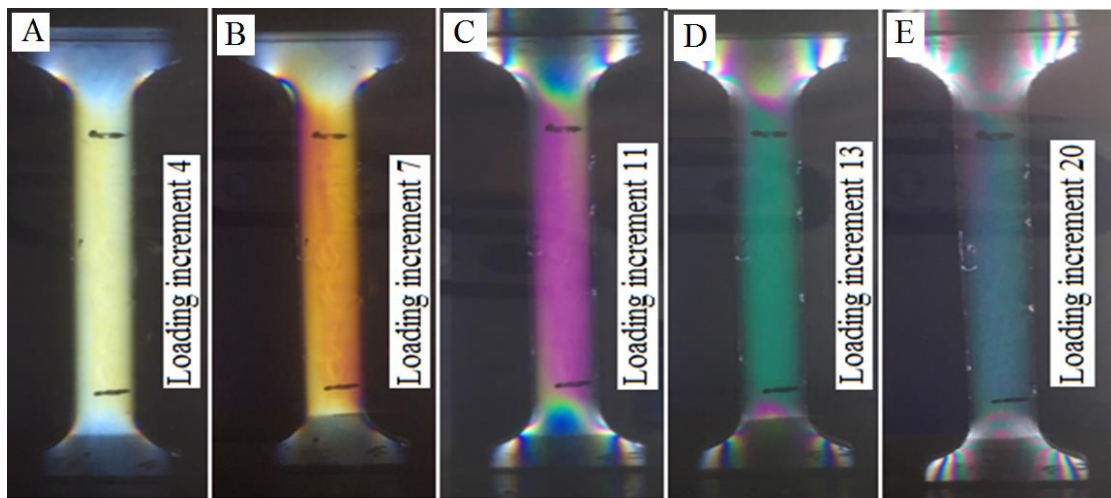


Figure 7: Stress-induced birefringence of sample 2 after different loading increments.

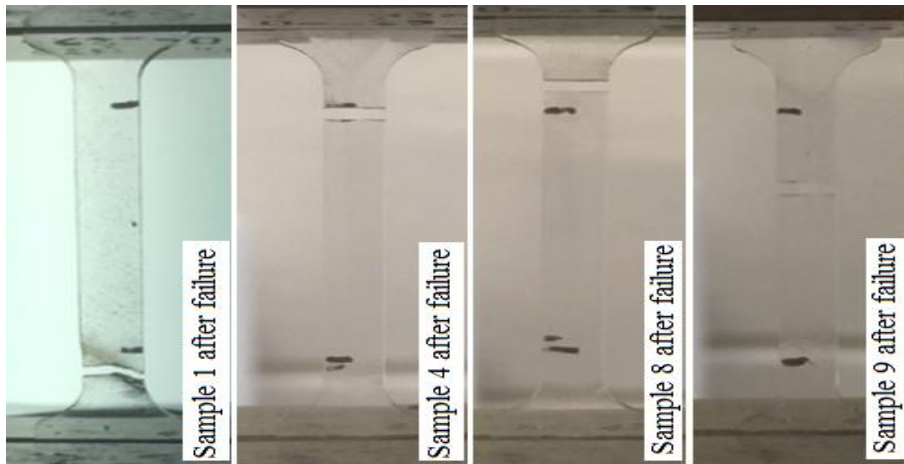


Figure 8: samples 1, 4, 8, and 9 (continuous loading) after failure

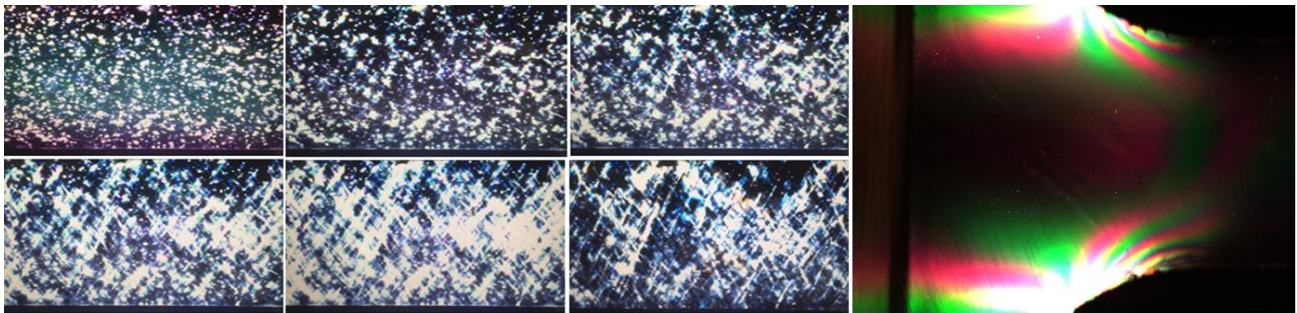


Figure 9: Sample 1 imperfections under different loads (Left), Stress-induced birefringent patterns in grip region of sample 2 (Right).

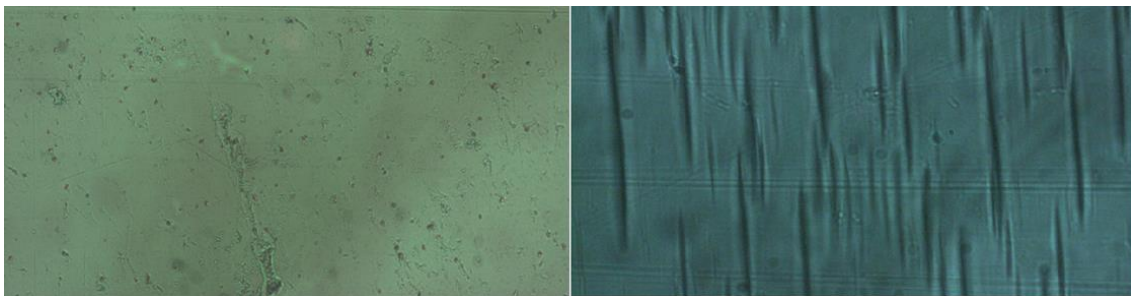


Figure 10: Sample surface before (left) and after (right) testing.

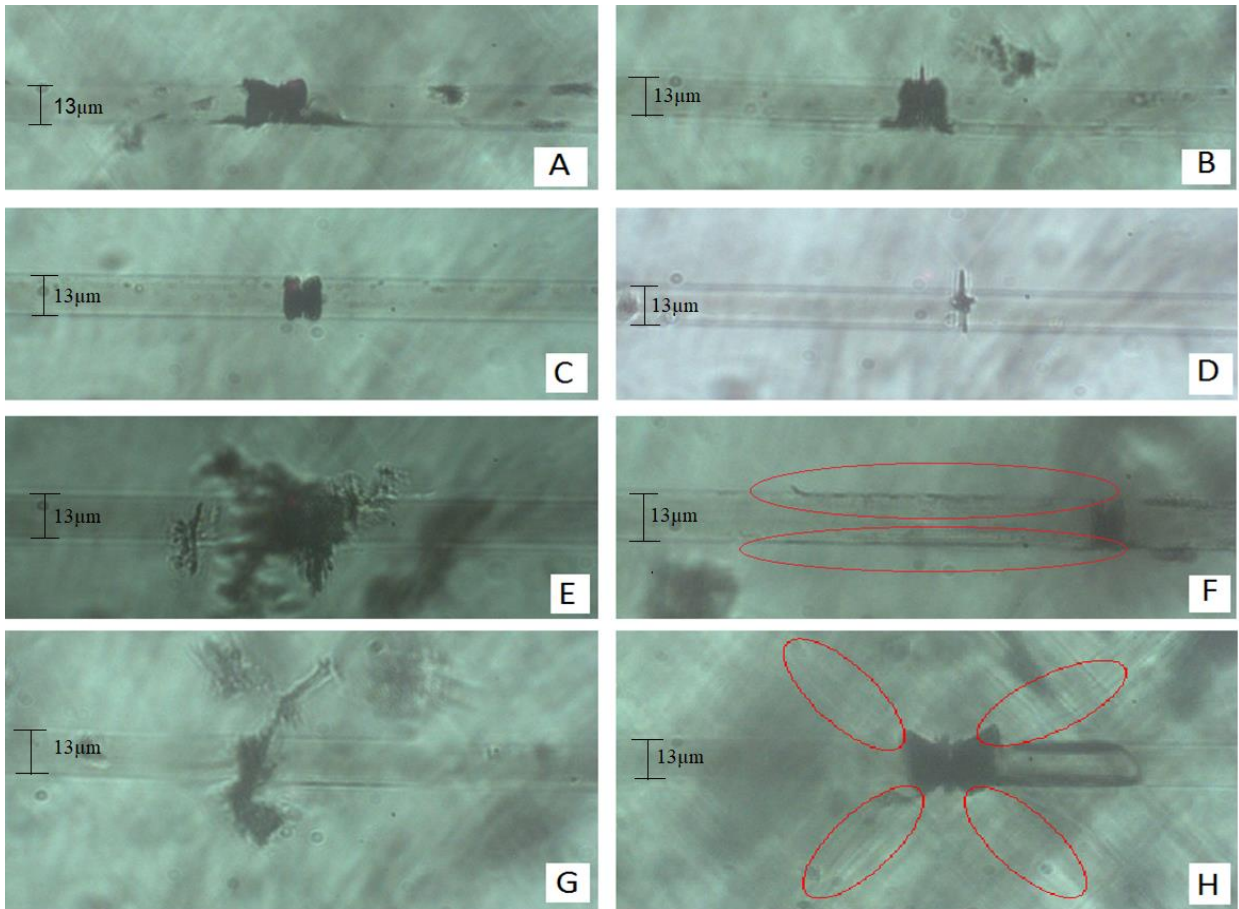


Figure 11: A) Failure mode (b) in sample 1 with some interfacial debonding, B) Failure mode (b) in sample 1 with small amount of interfacial debonding and slight transverse matrix crack, C) Failure mode (b) in sample 2, D) Failure mode (a) in sample 7, E) Failure mode (a) in sample 8 with crack propagation towards microscope lens, F) Failure mode (c) in sample 9, G) Failure mode (a) in sample 9, H) Failure mode (b) in sample 9 with moderate interfacial debonding.

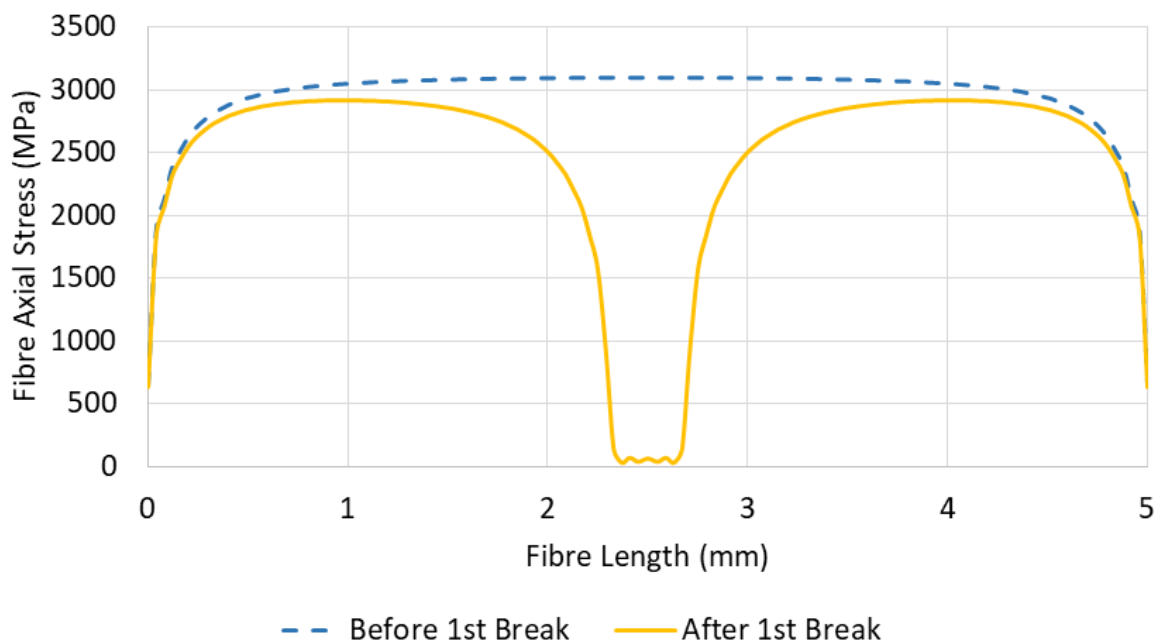


Figure 12: S11 stress in FE model (Left), FE predicted fibre axial stress (Right) before and after the first fibre break.

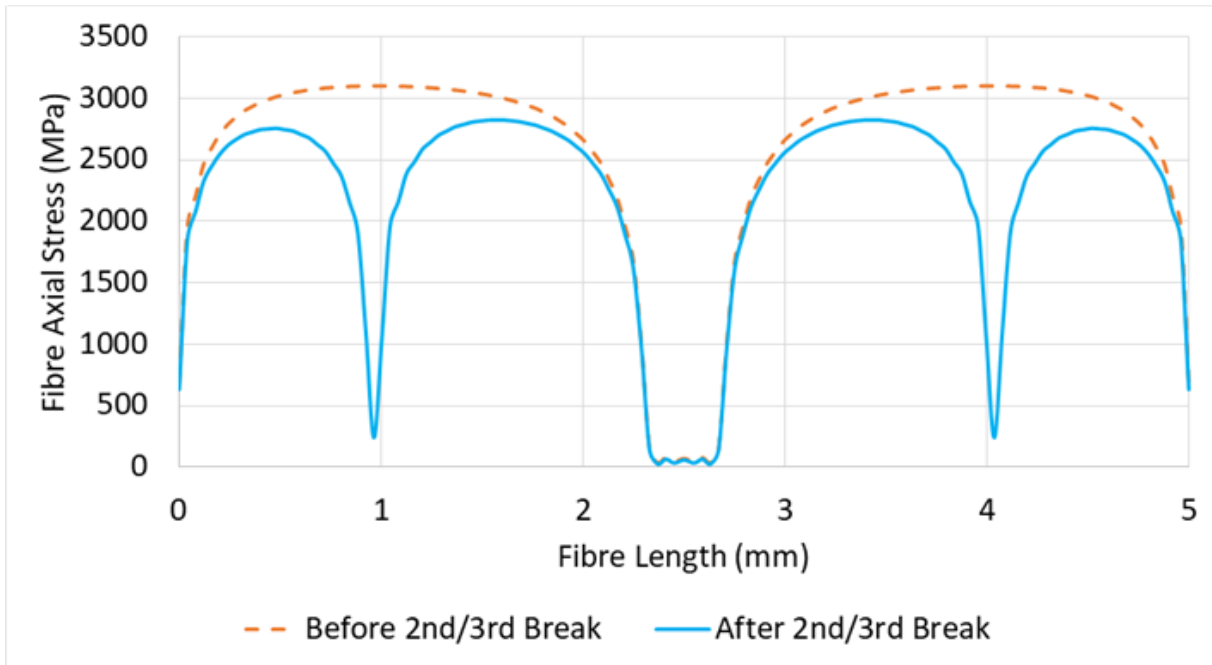


Figure 13: S11 stress in FE model (Left), FE predicted fibre axial stress (Right) before and after the second and third fibre breaks.

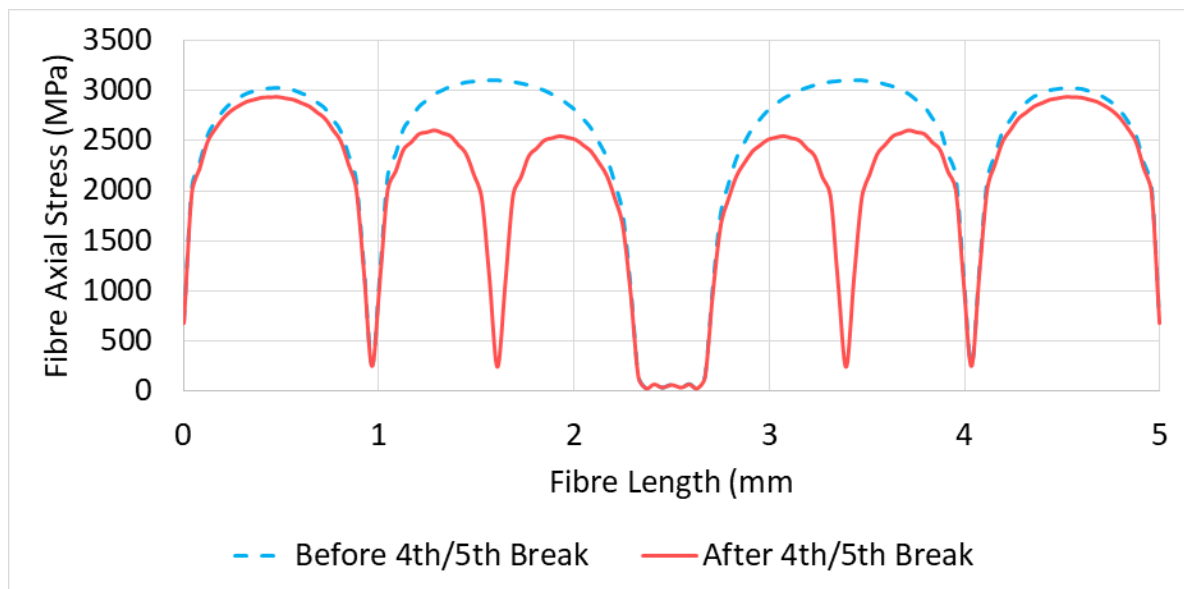


Figure 14: S11 stress in FE model (Left), FE predicted fibre axial stress (Right) before and after the fourth and fifth fibre breaks.

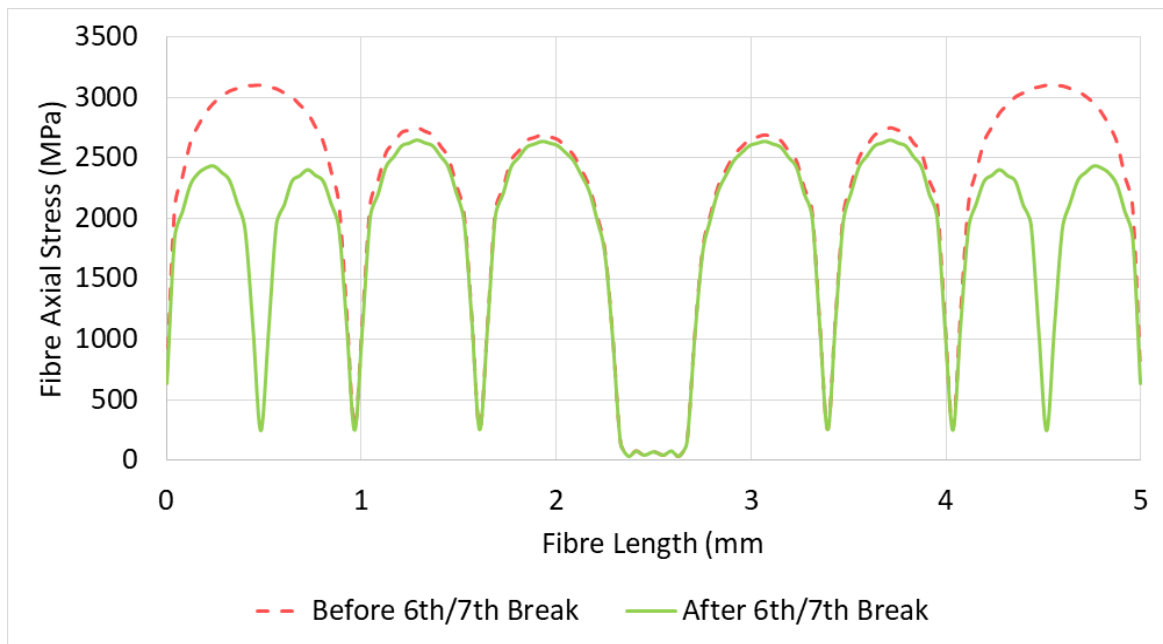


Figure 15: S11 stress in FE model (Left), FE predicted fibre axial stress (Right) before and after the sixth and seventh fibre breaks.

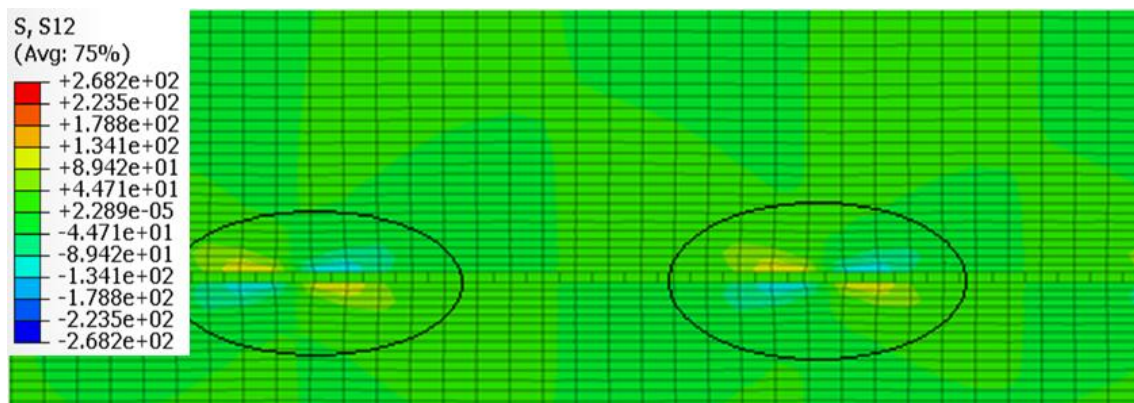


Figure 16: Close-up image of shear stresses about fibre fractures in FE model.

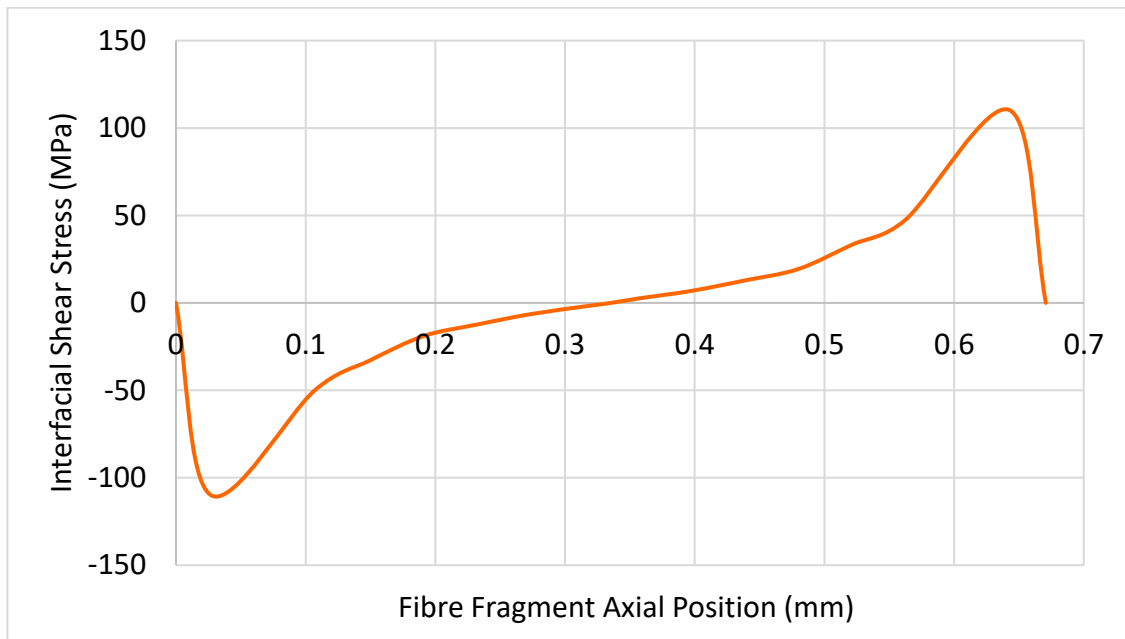


Figure 17: FE predicted interfacial shear stress distribution for fibre fragment.

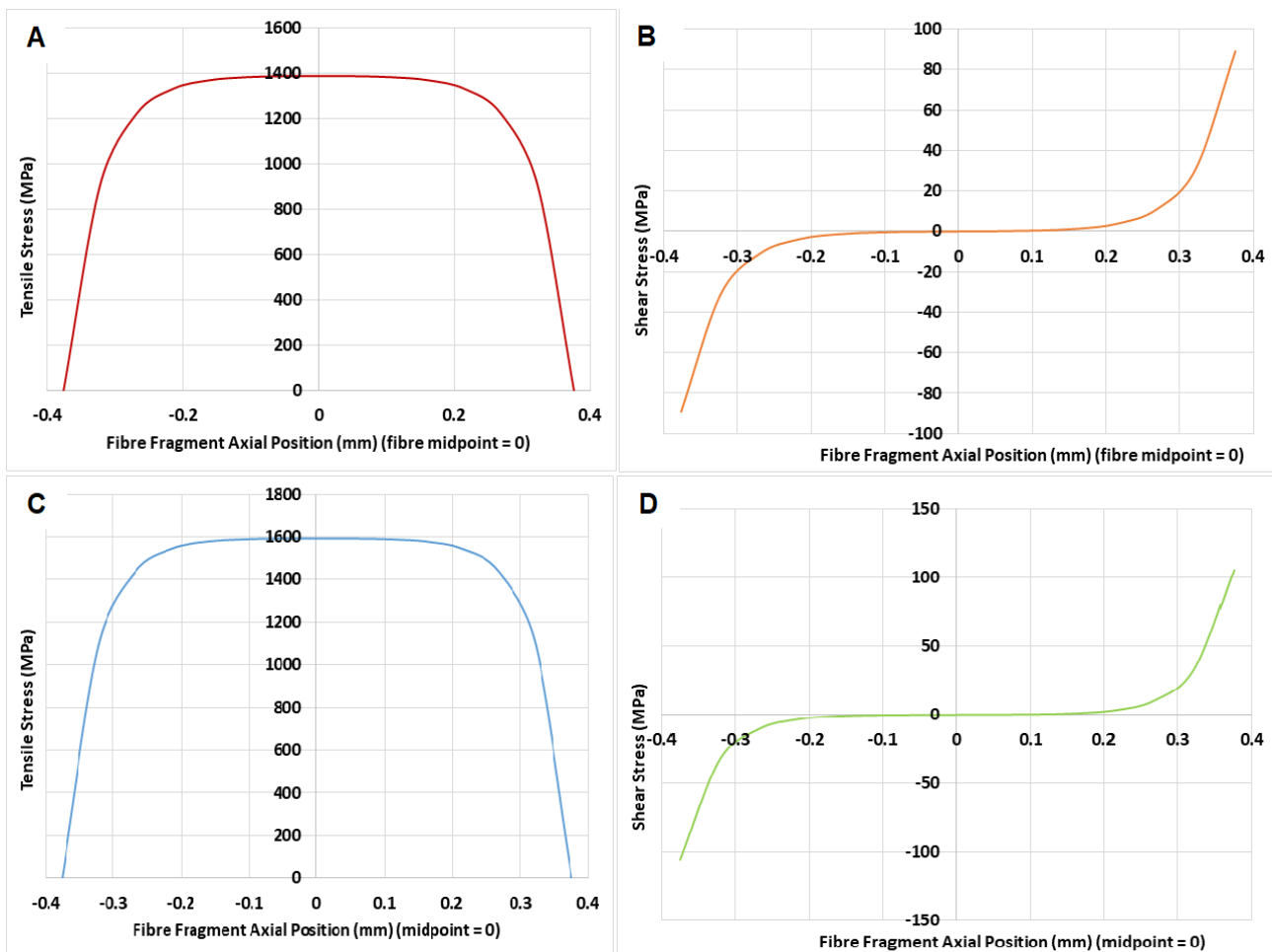


Figure 18: Theoretical prediction of fibre fragment tensile stress as a function of fibre axial position for sample 2 (A), sample 2 (B), sample 7 (C) and sample 7 (D).

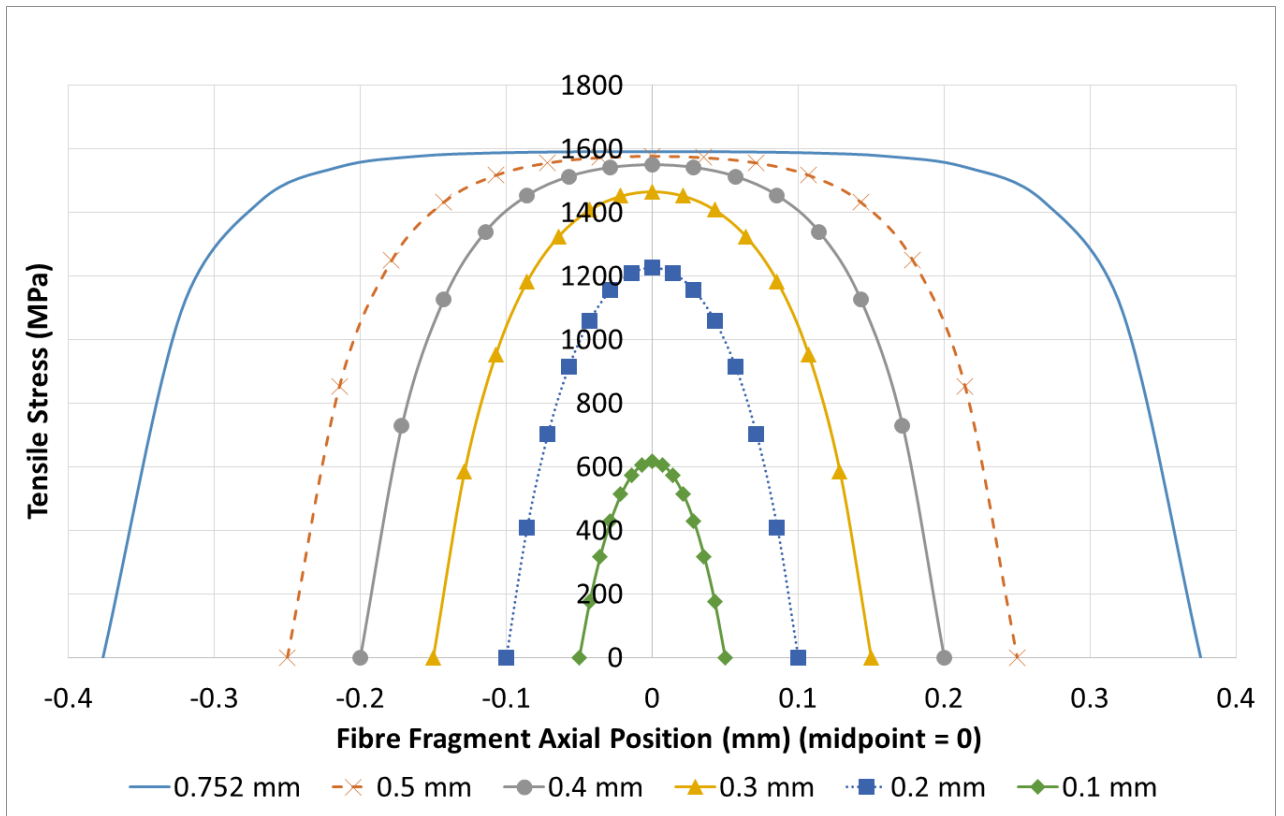


Figure 19: Axial stress distribution for fibres of various lengths.